

Richardson–Lucy Algorithm With Total Variation Regularization for 3D Confocal Microscope Deconvolution

NICOLAS DEY,¹ LAURE BLANC-FERAUD,^{1*} CHRISTOPHE ZIMMER,² PASCAL ROUX,³ ZVI KAM,⁴ JEAN-CHRISTOPHE OLIVO-MARIN,² AND JOSIANE ZERUBIA¹

¹Ariana Group, INRIA/I3S, 2004 route des Lucioles–BP93, 06902 Sophia Antipolis, France

²Quantitative Image Analysis Group, Institut Pasteur, 25–28 rue du Dr. Roux, 75015 Paris, France

³Dynamic Imaging Platform, Institut Pasteur, 25–28 rue du Dr. Roux, 75015 Paris, France

⁴Department of Molecular Cell Biology, Weizmann Institute of Science, Rehovot, Israel 76100

KEY WORDS image deconvolution; total variation regularization; Poisson noise; fluorescence confocal microscopy

ABSTRACT Confocal laser scanning microscopy is a powerful and popular technique for 3D imaging of biological specimens. Although confocal microscopy images are much sharper than standard epifluorescence ones, they are still degraded by residual out-of-focus light and by Poisson noise due to photon-limited detection. Several deconvolution methods have been proposed to reduce these degradations, including the Richardson–Lucy iterative algorithm, which computes maximum likelihood estimation adapted to Poisson statistics. As this algorithm tends to amplify noise, regularization constraints based on some prior knowledge on the data have to be applied to stabilize the solution. Here, we propose to combine the Richardson–Lucy algorithm with a regularization constraint based on Total Variation, which suppresses unstable oscillations while preserving object edges. We show on simulated and real images that this constraint improves the deconvolution results as compared with the unregularized Richardson–Lucy algorithm, both visually and quantitatively. *Microsc. Res. Tech.* 69:260–266, 2006. © 2006 Wiley-Liss, Inc.

INTRODUCTION

The confocal laser scanning microscope (CLSM) is an optical fluorescence microscope that uses a laser to scan and image point-by-point a sample in 3D, and where a pinhole is used to reject most out-of-focus light. The ability of the CLSM to image optical sections explains its widespread use in biological research. Nevertheless, the quality of confocal microscopy images still suffers from two basic physical limitations. First, out-of-focus blur due to the diffraction-limited nature of the optics remains substantial, even though it is reduced compared to epifluorescence microscopy. Second, the confocal pinhole drastically reduces the amount of light detected by the photomultiplier, leading to Poisson noise. The images produced by the CLSM can therefore benefit from postprocessing by deconvolution methods designed to reduce blur and noise.

Several deconvolution methods have been proposed for 3D microscopy. In wide-field microscopy, Agard and Sedat (1983) and many others achieved out-of-focus deblurring by constrained iterative deconvolution. For confocal images, Tikhonov–Miller inverse filter (van Kempen et al., 1997), Carrington (van Kempen and van Vliet, 2000a) and Richardson–Lucy (RL) algorithms (Lucy, 1974; Richardson, 1972) have also been applied. The latter has been used extensively in astrophysical or microscopic imaging (van Kempen et al., 1997), and is of particular interest for confocal microscopy, because it is adapted to Poisson noise. An important drawback of RL deconvolution, however, is that it does not converge to the solution because the noise is amplified after a small number of iterations. This sen-

sitivity to noise can be avoided with the help of regularization constraints, leading to much improved results. van Kempen et al. have applied a RL algorithm using energy-based regularization to biological images (van Kempen and van Vliet, 2000a). The term based on the Tikhonov–Miller expression suppresses noise amplification, but it has the drawback to smooth edges.

In this study, we propose to use the total variation (TV) as a regularization term. The main advantages of the TV are that it preserves the edges in the image and smoothes homogeneous areas. It has been proposed for 2D optical gray level image restoration in Rudin et al. (1992). This kind of nonlinear image restoration has been extensively used in image processing inverse problems, for the last 10 years, and has generated mathematical studies on the Bounded Variation (BV) function space (Ambrosio et al., 2000). In this study, we propose to apply this nonlinear regularization to the deconvolution of 3D confocal microscopy images. Considering the statistical Poisson nature of the noise, this leads to a RL algorithm with nonlinear regularization. The paper is organized as follows. The first section presents the image formation model, by describing the point spread function and the noise distribution. In the second section, we first recall the RL algorithm in

*Correspondence to: Laure Blanc-Feraud, Ariana Group, INRIA/I3S, 2004 route des Lucioles–BP93, 06902 Sophia Antipolis, France.
E-mail: Laure.Blanc_Feraud@sophia.inria.fr

Contract grant sponsors: INRIA ARC DéMiTri, P2R Franco-Israeli Program.

Received 28 July 2005; accepted in revised form 13 October 2005

DOI 10.1002/jemt.20294

Published online in Wiley InterScience (www.interscience.wiley.com).

the context of microscope imaging, and then describe the nonlinear TV regularized RL algorithm. Next, we present the results of the proposed algorithm on synthetic and real data, and compare them with the standard algorithm without regularization, both in terms of visual image quality and a numerical criterion. The last section concludes the paper.

IMAGE FORMATION MODEL

The image formation can be modeled with the Point Spread Function (PSF) and the statistical distribution of the detection noise. Such a general model can be written as:

$$i = \wp(o * h) \quad (1)$$

where i is the observed (measured) image, o is the object we want to retrieve (corresponding to the distribution of fluorescent markers inside the specimen), h is the PSF, and \wp models the noise distribution.

Noise

In a confocal microscope, a pinhole is used to reject most out-of focus light. The amount of light reaching the detector is therefore low, and the noise statistics is well described by a Poisson process. The distribution of i at point s , $i(s)$, knowing $(o * h)(s)$, is a Poisson distribution of the parameter $(o * h)(s)$:

$$P(i(s)/(o * h)(s)) = \frac{[(o * h)(s)]^{i(s)} e^{-(o * h)(s)}}{i(s)!} \quad (2)$$

Assuming that the noise is spatially uncorrelated, the statistics of the observed image i , knowing the object o , (and the PSF h which is considered here as a parameter) is the likelihood distribution given by:

$$P(i/o) = \prod_{s \in S} \left(\frac{[(o * h)(s)]^{i(s)} e^{-(o * h)(s)}}{i(s)!} \right) \quad (3)$$

where s is the coordinate of a 3D voxel and S is the total set of voxel coordinates in the imaged volume.

Confocal Point Spread Function

Under the assumptions of a translation invariant PSF, incoherent imaging, and monochromatic light (excitation and emission), we use a well-known image formation model of the CLSM, which has been proposed by van Kempen and van Vliet (1999), and is derived from Sheppard and Cogswell (1990). For a defocusing Z , the 3D PSF (Sheppard and Cogswell, 1990) is given by:

$$h(X, Y, Z) = |A_R(X, Y) * \hat{P}_{\lambda_{em}}(X, Y, Z)|^2 \times |\hat{P}_{\lambda_{ex}}(X, Y, Z)|^2 \quad (4)$$

where λ_{ex} and λ_{em} are the excitation and emission wavelengths, respectively. The pinhole (Born and Wolf, 1999; Goodman, 1996) is represented by $A_R(X, Y)$, and P_λ is the 2D Fourier transform of the pupil function P_λ

given by:

$$P_\lambda(U, V, Z) = \Pi_\rho \left(\sqrt{U^2 + V^2} \right) e^{\frac{2i\pi}{\lambda} W(U, V, Z)} \quad (5)$$

Here $W(U, V, Z) = \frac{1}{2}Z(1 - \cos 2\alpha)$ is the aberration phase derived from Goodman(1996). It gives a measure of the wavefront path difference between a focused and a defocused beam (Born and Wolf, 1999; Stokseth, 1969). $\rho = \frac{NA}{2\lambda}$ is the lateral cutoff frequency, and $NA = n_o \sin \alpha$ the numerical aperture, which is related to the cone of light collected by the objective and the immersion medium refractive index n_o . The model takes into account the finite size of the pinhole, which is used for the image acquisition. This PSF model will be used both for the creation of the simulated images and for the deconvolution.

In van Kempen and van Vliet (1999) and van Kempen and van Vliet, (2000a), the authors use an image formation model for confocal microscopy, which is slightly different from Eq. (1): namely $i = \rho(o * h + b)$, where b models the background signal. In a previous work (Dey et al., 2004a,b), we showed that the use of a background term in the model is not necessary if a well suited regularization term is included. In fact, it happens that using a background model is equivalent to imposing a support constraint to regularize the solution. We also showed that when using a regularization term, no improvement is reached by adding the background term, and that it is therefore not needed.

CONFOCAL MICROSCOPY IMAGE DECONVOLUTION

The Multiplicative RL Algorithm

The RL algorithm finds o from the observation i , knowing the PSF h , by maximizing the likelihood distribution (Eq. (3)) with respect to o . The RL algorithm can be derived by using the Expectation–Maximization (EM) algorithm (Dempster et al., 1977), or by minimizing the functional $-\log p(i|o)$, using a multiplicative type algorithm. Let us briefly describe the second approach. Minimizing $-\log p(i|o)$ is equivalent to minimizing $J_1(o)$ given by:

$$J_1(o) = \sum_s (-i(s) \log[(o * h)(s)] + (o * h)(s)) \quad (6)$$

Since the functional $J_1(o)$ is convex in o , searching for a minimum is equivalent to searching for a zero of the gradient of $J_1(o)$ which results in solving

$$\left[\frac{i(s)}{(o_k * h)(s)} \right] * h(-s) = 1 \quad (7)$$

Let $o_k(s)$ be the estimate of o at iteration k . Then one iteration of a multiplicative gradient type algorithm (for more details see Lucy (1974) and Richardson 1972) or Appendix C of Dey et al. (2004a)) is given by:

$$o_{k+1}(s) = \left\{ \left[\frac{i(s)}{(o_k * h)(s)} \right] * h(-s) \right\} o_k(s) \quad (8)$$

which defines one iteration of the RL algorithm. An important property of this scheme is that it ensures nonnegativity if the first estimate (here taken as the measured 3D image, scaled by a value equal to the mean of the image stack) is nonnegative. However, because the inversion problem is ill-posed and the Maximum Likelihood (ML) estimator is nonregularized, the solution given by Eq. (8) when $k \rightarrow +\infty$ consists of noise only, because of noise amplification. To obtain good results, the algorithm is stopped before the noise is amplified. In order to improve the trade-off between a good deconvolution with sharp edges and noise amplification, we propose to regularize the solution by minimizing its TV.

Total Variation Regularization

In a Bayesian approach, a regularization is obtained by Maximizing the a posteriori distribution (MAP estimator) $P(o/i) = P(i/o) \times P(o)/P(i)$ with a suitable a priori distribution $P(o)$. Tikhonov–Miller (TM) (van Kempen and van Vliet, 1999; van Kempen and van Vliet, 2000b) regularization is the most popular algorithm in 3D image deconvolution. TM regularization is designed to avoid noise amplification by smoothing, causing smear of the object edges. de Monvel et al., (2003) used a RL algorithm with maximum entropy regularization. This regularization gives better results than that of TM regularization, in the sense that the edges are less smoothed. However, the trade-off between good regularization with a good reduction of the noise, and edge preservation still exists. This compromise can be improved by using wavelet coefficient thresholding, as proposed by de Monvel et al. (2003).

Here, we introduce an other a priori constraint on the object by adding to the energy J_1 , a regularization term J_{reg} , defined by the TV of the solution o as in Rudin et al. (1992):

$$J_{\text{reg}}(o) = \lambda_{\text{TV}} \sum_s |\nabla o(s)| \quad (9)$$

The total functional to be minimized is then:

$$J_1(o) + J_{\text{reg}}(o) = \sum_s (-i(s) \log[(o * h)(s)] + (o * h)(s)) + \lambda_{\text{TV}} \sum_s |\nabla o(s)| \quad (10)$$

Using the \mathcal{L}^1 norm over ∇_o rather than the \mathcal{L}^2 norm as in TM regularization (van Kempen and van Vliet, 2000b) allows to recover a smooth solution with sharp edges. It can be shown (Rudin et al., 1992) that the smoothing process introduced by J_{reg} acts only in the direction tangential to the image level lines and not in the orthogonal direction, so that edges are preserved. The derivative of J_{reg} with respect to o is a nonlinear term $\frac{\partial}{\partial o} J_{\text{reg}} = -\lambda_{\text{TV}} \text{div} \left(\frac{\nabla_o}{|\nabla_o|} \right)$ where div stands for the divergence. We minimize Eq. (10) using the multiplicative gradient-based algorithm (or equivalently by using EM algorithm for the penalized criterion of Eq. (10)), and we adopt an explicit scheme, as in Green

(1990), defined by:

$$o_{k+1}(s) = \left\{ \left[\frac{i(s)}{(o_k * h)(s)} \right] * h(-s) \right\} \times \frac{o_k(s)}{1 - \lambda_{\text{TV}} \text{div} \left(\frac{\nabla_{o_k}(s)}{|\nabla_{o_k}(s)|} \right)} \quad (11)$$

Numerically we noticed that the regularization parameter λ_{TV} should be neither too small nor too large: if $\lambda_{\text{TV}} < 10^{-6}$, RL is dominated by the data model; if $\lambda_{\text{TV}} \sim 1$, RL is dominated by the regularization term. For larger λ_{TV} , the denominator of Eq. (8) can become zero or negative. This must be avoided because small denominators create points of very high intensity, which are amplified at each iteration. A negative value violates the nonnegativity constraint. We use a parameter $\lambda_{\text{TV}} = 0.002$ for computations, and iterations are stopped at convergence, defined when the relative difference between two images is less than a threshold (10^{-5} in the experiments presented below).

RESULTS

Evaluation Criteria

In the following, we report results on three synthetic (simulated) objects and two types of real specimens. To quantify the quality of the deconvolution we used the I-divergence criterion, which is the best measure in the presence of a nonnegativity constraint (Csisz  r, 1991). The I-divergence between two 3D images A and B is defined by:

$$I_{A,B} = \sum_{s \in S} \left\{ A_s \ln \left[\frac{A_s}{B_s} \right] - (A_s - B_s) \right\} \quad (12)$$

The I-divergence is nonsymmetric, i.e., $I_{A,B} \neq I_{B,A}$. In the experiments with synthetic data, image A is the known undegraded initial image (the one we want to retrieve) and image B is the restored one. The I-divergence then quantifies the difference between the ideal image and the reconstructed one. Ideally, a perfect deconvolution should end with I-divergence equal to zero. This numerical criterion cannot be computed on results from real data because the undegraded object is not known.

In order to display the visual quality, we present cross sections of the objects before and after deconvolution with the RL algorithm and with the TV regularized RL algorithm.

Results on Synthetic Data

We show results on three different synthetic objects, shown in Figures 1–3 (column a). These objects are artificially blurred and corrupted by Poisson noise using the image formation model described in the section of image formation model. The resulting degraded images are shown in Figures 1–3 (column b). Deconvolution results of the degraded images using standard RL are shown in Figures 1–3 (column c). For standard RL, we used the number of iterations that achieves minimum I-divergence. The deconvolution results

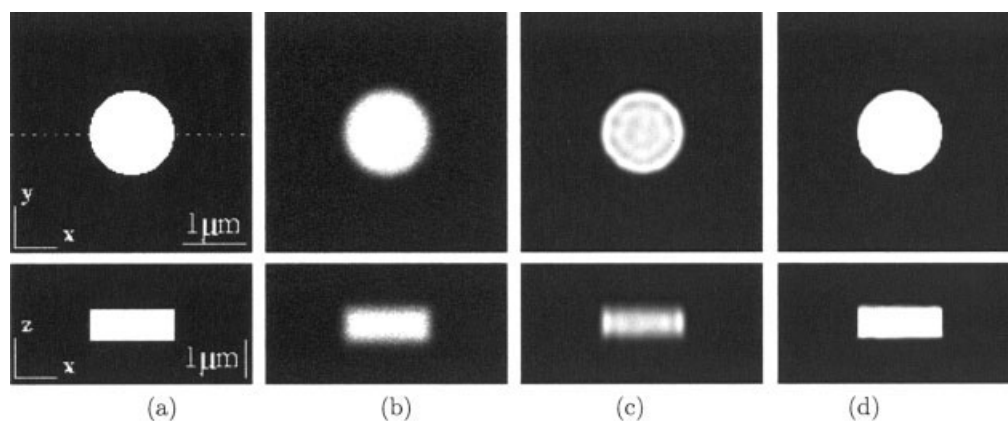


Fig. 1. Deconvolution of a binary cylinder. (a) the original 3D synthetic image; (b) the same image, degraded by blur and Poisson noise according to the image formation model; (c) deconvolution by standard RL (I-divergence is 0.766); (d) deconvolution by RL-TV with $\lambda_{TV} = 0.002$ (I-divergence is 0.220). The top row shows the lateral (XY)

section through the center of the image stack. The bottom row shows the axial (YZ) section corresponding to the dotted line shown in (a). The image size is $128 \times 128 \times 64$ with voxel size $30 \times 30 \times 50$ nm in X, Y, and Z.

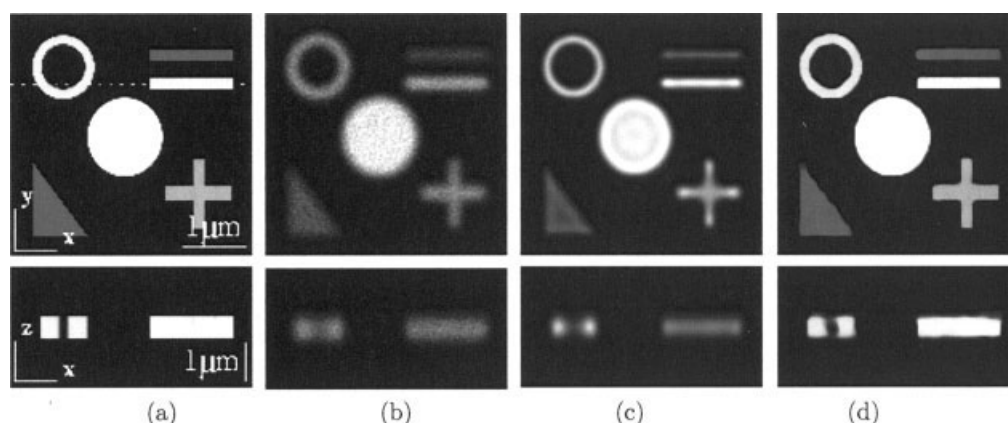


Fig. 2. Deconvolution of a composite image. (a) original image; (b) degraded by blur and Poisson noise; (c) deconvolved with standard RL; (d) deconvolved with RL-TV. The objects exhibit different intensities: 255 for the cylinder, 221 for the annulus, 170 for the cross, 102

for the triangle, 238 and 102 for the two bars, 10 for the background. Final I-divergence is 1.365 for standard RL (c) and 0.691 for RL-TV with $\lambda_{TV} = 0.002$ (d). The size of the stack is $128 \times 128 \times 64$ with voxel size $30 \times 30 \times 50$ nm in X, Y, and Z.

using RL with TV regularization (RL-TV) are shown in Figures 1–3(column d).

The first simulated object is a full cylinder (Fig. 1a). It is a single object, presenting no corner (except at the top and bottom) and which is homogeneous (there are only two intensity values: the background and the cylinder). Figure 1c shows the result of the deconvolution using the standard RL algorithm: in lateral and axial views there is still some blur, and intensity oscillation artifacts are clearly apparent. The RL-TV algorithm greatly improves the results (Fig. 1d): the cylinder is sharp (the edges are sharp in lateral and axial views) and there are no intensity oscillations (see the corresponding intensity profile in Figure 6a). The axial view shows that the heights of the deconvolved cylinder (Fig. 1d) and of the initial cylinder (Fig. 1a) are similar. The final I-divergence is 0.766 for standard RL and 0.220 for RL-TV, resulting in a more than 3-fold improvement.

Figure 2a presents another 3D synthetic image composed of five geometrical shapes. These are more complex objects with corners and homogeneous regions of different intensity levels. The deconvolution result, with

standard RL, is shown in Figure 2c. The different shapes are still blurred and appear thinner than before degradations. Many intensity oscillations appear inside the shapes. All of these artifacts are avoided when using the RL-TV algorithm (Fig. 2d): all shapes are sharp, the thickness is preserved, and there are no more intensity oscillations (see the intensity profile in Fig. 6b). The cross-section displays a slight effect of rounding corners. In the axial view, the borders are not perfectly sharp. Nevertheless, the final I-divergence is 0.691 for the proposed method, which represents nearly a 2-fold improvement compared with standard RL (1.365).

In Figure 3a, we present a 3D synthetic object combining texture and fine structures. The object is inhomogeneous and the fine structure exhibits sharp transitions. The degradation (Fig. 3b) is sufficiently strong to almost hide these details. The deconvolution obtained with standard RL still shows strong axial blur. With RL-TV, this blur is almost completely removed, and the fine structures are discernable again. However, a drawback of TV regularization is apparent on the XY section: a stair-casing effect. It is due to the nonderiv-

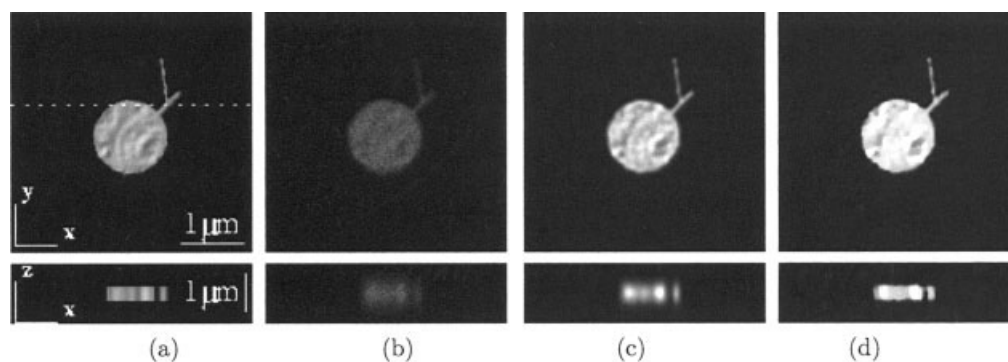


Fig. 3. Deconvolution of a textured image with fine structure. (a) original image; (b) degraded by blur and Poisson noise; (c) deconvolved with standard RL; (d) deconvolved with RL-TV. Final I-divergence is 0.462 for standard RL (c) and 0.404 for RL-TV with $\lambda_{TV} = 0.002$ (d). Note that axial blur is much reduced with RL-TV compared to RL. The image size is $128 \times 128 \times 32$.

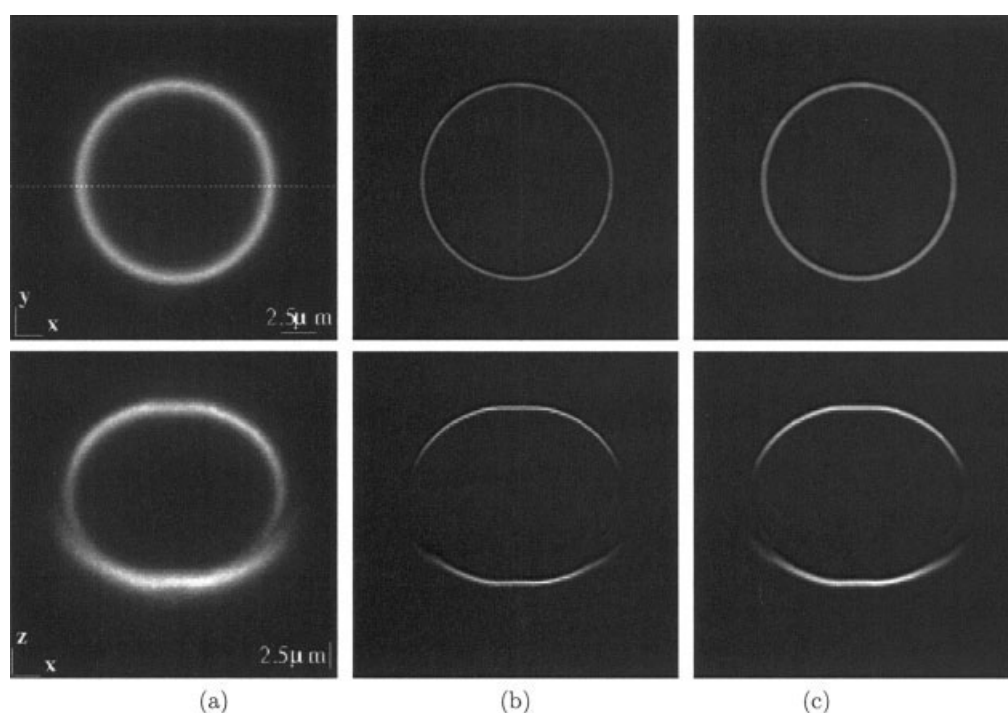


Fig. 4. Deconvolution of a spherical shell image. (a) shows the raw image, (b) the result of standard RL deconvolution, (c) the result of RL-TV deconvolution, with $\lambda_{TV} = 0.002$. RL-TV deconvolution allows a better estimate of the shell thickness than RL (see text). The image size is $256 \times 256 \times 128$ with voxel size $89 \times 89 \times 230$ nm in X, Y, and

Z. First row represents the central XY image, and second line the central axial section of this stack corresponding to the dotted line. There is no resampling to obtain the same scale in X, Y, and Z, only a resizing of the image.

ability of the absolute value in zero, and appears mainly in parts of the image which contain oscillations of small amplitudes, as textures. The intensity profiles in Figure 6c do not show significant differences between standard RL and RL-TV results. Final I-divergence is 0.462 for standard RL and 0.404 for RL-TV, which is an improvement by 12.6%.

Results on Real Data

To evaluate the performances of our method on real data, we chose two types of objects, beads and shells, whose size and shape are well characterized and which can therefore be used as bona fide references. The

beads are FocalCheckTM F-24634 (Molecular Probes) fluorescent microspheres, with a diameter of 6 μm . The shells are 15 μm in diameter, with a fluorescent layer of thickness between 0.5 and 0.7 μm . The fluorescence excitation wavelength is $\lambda_{ex} = 488$ nm; the emission wavelength is $\lambda_{em} = 520$ nm; the pinhole size was set to 1 Airy unit; in object space, the XY dimension of each voxel was 89 nm and the Z dimension 230 nm. The microscope was a Zeiss LSM 510, equipped with an immersion oil Apochromat 63 \times with numerical aperture NA = 1.4 objective, and an internal magnification of 3.3 \times . Image acquisition was performed using the Zeiss Vision software.

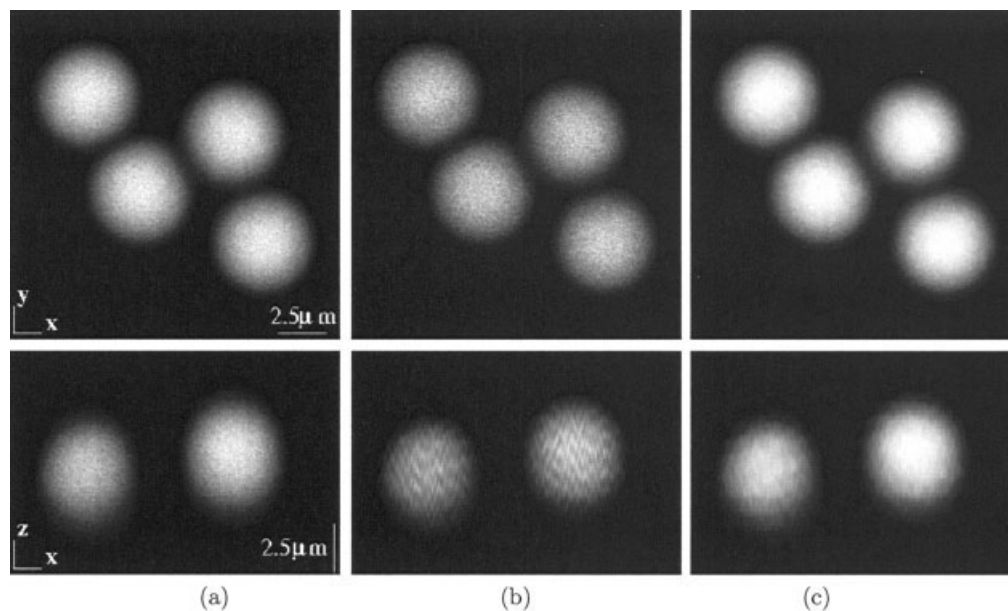


Fig. 5. Deconvolution of a bead cluster image. (a) original image; (b) deconvolved with standard RL; (c) deconvolved with RL-TV. The result of RL deconvolution (b) presents a high level of noise and the axial view shows oscillation artifacts. These degradations are much reduced with RL-TV deconvolution ($\lambda_{TV} = 0.005$). The stack size is $256 \times 256 \times 128$ with voxels of size $89 \times 89 \times 230$ nm.

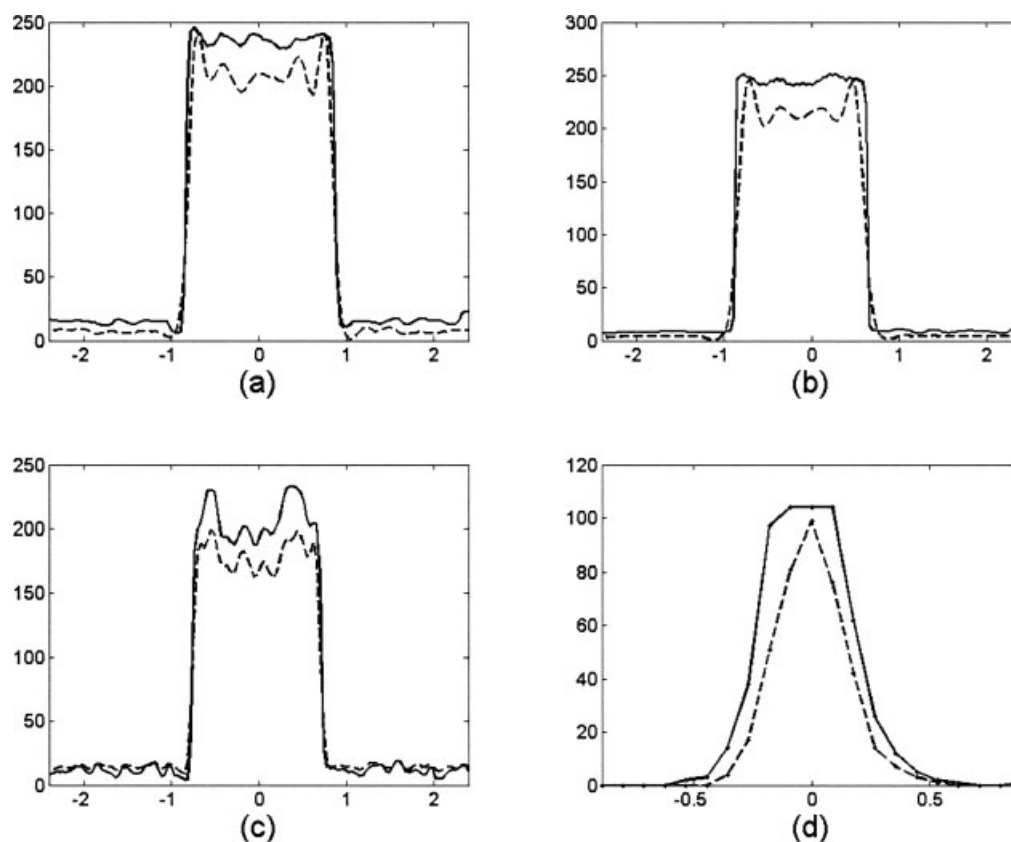


Fig. 6. Intensity profiles of four test images. In each panel, the dashed curve corresponds to images deconvolved with standard RL, and the solid curve corresponds to images deconvolved with RL-TV. (a) intensity profile of the synthetic cylinder image (Fig. 1); (b) profile of the synthetic composite image (Fig. 2); (c) profile of the textured

synthetic object with fine structure (Fig. 3). The profile corresponds to a section in the middle of the object; (d) profile of the real spherical shell image (Fig. 4). We show only a profile through the right part of the shell. Note that RL-TV deconvolution produces a sharper profile than standard RL. Values on the horizontal axes are in microns.

The results of applying the deconvolution algorithm to a spherical shell image are shown in Figure 4. The improvements achieved with RL-TV are a better localization of the borders and a better estimation of the shell thickness. In Figure 6d, we show a zoom of the intensity profiles through the right portion of the shell image deconvolved with standard RL and RL-TV. These profiles can be used to estimate the thickness of the shell. On the raw image data (Fig. 4a), we measured a shell thickness of $0.93\ \mu\text{m}$, which is larger than the true thickness; on the result of RL deconvolution (Fig. 4b), the measured thickness is $0.26\ \mu\text{m}$, which is too small. The thickness measured using RL-TV deconvolution (Fig. 4c), is $0.40\ \mu\text{m}$ and thus also too small, but this value lies closer to the real thickness (between 0.5 and $0.7\ \mu\text{m}$).

We also tested the proposed deconvolution algorithm on a cluster of beads of diameter $6\ \mu\text{m}$ (Fig. 5). For the deconvolution with RL-TV, we used a regularization parameter $\lambda_{\text{TV}} = 0.005$. The improvement of RL-TV deconvolution compared to standard RL can be appreciated in Figure 5c, as most of the blur has been removed, and the artifacts produced by standard RL deconvolution (visible in the X-Z view of Fig. 5b) are no longer present.

CONCLUSION

In this paper, we have presented a new deconvolution approach for 3D confocal microscopy. It is based on the RL algorithm that is regularized using the TV. RL with no regularization suffers from unstable noise amplification. Many authors have proposed to regularize the energy using different functionals. Tikhonov-Miller functional is often used, but it over-smoothes the edges of objects in the image. We have proposed to use a regularization term based on Total Variation, which is non quadratic and does not smooth edges. We have presented results on simulated and real data that demonstrate, both in qualitative and in quantitative terms, the advantage of the RL-TV algorithm over its nonregularized version.

REFERENCES

- Agard D, Sedat J. 1983. Three-dimensional architecture of a polytene nucleus. *Nature* 302:676–681.
- Ambrosio L, Fusco N, Pallara D. 2000. Functions of bounded variation and free discontinuity problems. Oxford: Oxford University Press.
- Born M, Wolf E. 1999. Principles of optics, 7th ed. Cambridge, UK: Cambridge University Press.
- Csiszár I. 1991. Why least squares and maximum entropy? *The Ann Stat* 19:2032–2066.
- Dempster A, Laird N, Rubin D. 1977. Maximum Likelihood from incomplete data via the EM algorithm. *J Roy Stat Soc B* 39:1–38.
- Dey N, Blanc-Féraud L, Zimmer C, Roux P, Kam Z, Olivo-Marin JC, Zerubia J. 2004a. 3D microscopy deconvolution using Richardson-Lucy algorithm with total variation regularization. INRIA Technical Report 5272.
- Dey N, Blanc-Féraud L, Zimmer C, Kam Z, Olivo-Marin JC, Zerubia J. 2004b. A deconvolution method for confocal microscopy with total variation regularization. In: Proceedings of IEEE International Symposium on Biomedical Imaging (ISBI), April 2004.
- Goodman JW. 1996. Introduction to Fourier optics, 2nd ed. New York: McGraw-Hill.
- Green P. 1990. On use of the EM algorithm for penalized likelihood estimation. *J Roy Stat Soc B* 52:443–452.
- van Kempen G, van Vliet L. 1999. The influence of the background estimation on the superresolution properties of nonlinear image restoration algorithms. In: Cabib D, Cogswell CJ, Conchello J-A, Lerner JM, Wilson T, editors. Three-dimensional and multidimensional microscopy: image acquisition and processing IV, Proceedings of the SPIE Conference, vol. 3605; pp. 179–189.
- van Kempen G, van Vliet L. 2000a. Background estimation in nonlinear image restoration. *J Opt Soc Am A* 17:425–433.
- van Kempen G, van Vliet L. 2000b. The influence of the regularization parameter and the first estimate on the performance of Tikhonov regularized nonlinear image restoration algorithms. *J Microsc* 198:63–75.
- van Kempen G, van Vliet L, Verveer P, van der Voort H. 1997. A quantitative comparison of image restoration methods for confocal microscopy. *J Microsc* 185:354–365.
- Lucy L. 1974. An iterative technique for rectification of observed distributions. *Astron J* 79:745–765.
- de Monvel JB, Scarfone E, Calvez SL, Ulfendahl M. 2003. Image-adaptive deconvolution for three-dimensional deep biological imaging. *Biophys J* 85:3991–4001.
- Richardson WH. 1972. Bayeslan-based iterative method of image restoration. *J Opt Soc Am* 62:55–59.
- Rudin LI, Osher S, Fatemi E. 1992. Nonlinear total variation noise removal algorithm. *Physica D* 60:259–266.
- Sheppard C, Cogswell C. 1990. Three-dimensional image formation in confocal microscopy. *J Microsc* 159:179–194.
- Stokseth P. 1969. Properties of a defocused optical system. *J Opt Soc Am* 59:1314–1321.